Mitochondrial ACSS1 Links Acetate Metabolism to Pyrimidine Biosynthesis in Nutrient-Stressed B-Cell Lymphomas

Johnvesly Basappa[1*], Aaron R. Goldman[2], Cosimo Lobello[1], Shengchun.Wang[1], David Rushmore[1], Olga Melnikov[1], Neil V. Sen[1], Vinay S. Mallikarjuna[1], Priyanka Jain[1], Masoud Edalati[1], Kathy Q. Cai[1], Pin Lu[1], Reza Nejati[1], Hossein Borghaei[1], Kathryn E. Wellen[3] and Mariusz A. Wasik[1]

[1]Fox Chase Cancer Center, Philadelphia, PA, USA

[2]Proteomics & Metabolomics Facility, Wistar Institute, Philadelphia, PA, USA Philadelphia, PA

[3]Department of Cancer Biology, University of Pennsylvania Perelman School of Medicine, Philadelphia, PA, USA.

Short title: ACSS1 Overexpression Drives Acetate-Dependent Metabolic Reprogramming in MCL

Keywords: *ACSS1*, ACSS2, ACLY, CAD, DHODH, acetate metabolism, oncometabolite, cancer metabolism,

*** Corresponding author:**

Johnvesly Basappa, Ph.D.

Department of Pathology, Fox Chase Cancer Center, Philadelphia, PA

Email: Johnvesly.Basappa@fccc.edu

Phone: 215-728-3039

Abstract

Acetate serves as an alternative carbon source in nutrient-limited tumors, yet its role in supporting nucleotide biosynthesis remains poorly understood. Here, we identify the mitochondrial enzyme ACSS1 as a key metabolic driver in mantle cell lymphoma (MCL), diffuse large B-cell lymphoma (DLBCL), and chronic lymphocytic leukemia (CLL). ACSS1 is frequently overexpressed and catalyzes the conversion of acetate to mitochondrial acetyl-CoA, sustaining oxidative metabolism and biosynthesis under nutrient stress. Genetic silencing of ACSS1 impairs mitochondrial respiration and disrupts acetate incorporation into acetyl-CoA, TCA cycle intermediates, glutamate, and aspartate, while markedly reducing ^{13}C-acetate labeling of dihydroorotate and orotate, intermediates in de novo pyrimidine synthesis. Untargeted metabolomics reveal enrichment of pyrimidine biosynthesis pathways in ACSS1-high cells. Notably, acetate or uridine supplementation rescues the growth of ACSS1-deficient cells, confirming a functional link between acetate metabolism and nucleotide synthesis. These findings uncover an ACSS1-dependent mitochondrial acetate–pyrimidine axis that sustains lymphoma growth and represents a potential therapeutic vulnerability.

Statement of significance:

This study identifies ACSS1 as a key metabolic vulnerability in mantle cell lymphoma (MCL), linking mitochondrial acetate metabolism to de novo pyrimidine biosynthesis. We demonstrate that ACSS1 is frequently overexpressed in MCL and is essential for converting acetate into mitochondrial acetyl-CoA, sustaining TCA cycle activity, nucleotide production, and cell survival under nutrient stress. Loss of ACSS1 disrupts this acetate–pyrimidine axis, impairing mitochondrial metabolism and reducing lymphoma cell viability. Importantly, acetate or uridine supplementation rescues the growth of ACSS1-deficient cells, highlighting a direct metabolic link with therapeutic potential. These findings reveal a novel mechanism of metabolic adaptation in MCL and suggest that targeting ACSS1-mediated acetate utilization could offer a new therapeutic approach for treating aggressive, metabolically stressed lymphomas.

Introduction

In higher vertebrates, the swift growth of cells mainly relies on the intake of glucose and glutamine(1). Acetate is another nutritional source vital for the progression of many cancers, which often exhibit dysregulated metabolism, and it is essential under nutrient-deprived conditions(2). The mitochondrial acetyl-CoA synthetase short-chain family member 1 (ACSS1) catalyzes acetate, an energy source during nutrient deprivation conditions, to produce mitochondrial acetyl-CoA(2, 3). A recent study suggests that acetate promotes PD-L1 expression and immune evasion by upregulating c-Myc(4). Indeed, in ketogenic conditions, such as prolonged fasting or diabetes, the liver also generates sufficient quantities of acetate and releases it into the bloodstream(5). Mammals have three isoforms of the short-chain acetyl-CoA synthetases family: ACSS1, ACSS2, and ACSS3, which convert acetate into acetyl-CoA(6, 7), which is essential for cell growth and proliferation(8, 9). ACSS1 and ACSS3 localize in the mitochondria, while ACSS2 is found in the nucleus and cytoplasm(10). Among the three isoforms, ACSS2's role in acetate metabolism and cancer progression has been extensively studied in various types of cancer, including pancreatic cancer(11), hepatocellular carcinoma(12, 13), glioblastoma(14), breast cancer(15), prostate cancer(15), bladder cancer(16) and cervical squamous cell carcinoma(17). ACSS1 plays a crucial role in thermogenesis during fasting, in low-glucose or ketogenic states, and is vital for survival(18). The expression of ACSS1 is regulated in an estrogen receptor-dependent manner, and the estrogen hormone plays a role in regulating the incorporation of acetate into DNA(19, 20). In highly oxygen-rich environments, the majority of acetyl-CoA is generated from glucose pathways. Conversely, during low oxygen conditions, acetate serves as a source for acetyl-CoA production(21). The exact function of mitochondrial ACSS1 in acetate metabolism within lymphoma remains unknown.

Mantle cell lymphoma (MCL) is a type of B-cell lymphoma, characterized by a median overall survival of just 3-5 years years(22). While a subset of patients with mantle cell lymphoma (MCL) initially respond to Bruton tyrosine kinase (BTK) inhibitors, resistance, either intrinsic or acquired is a common clinical challenge. Emerging evidence suggests that metabolic reprogramming toward oxidative phosphorylation (OXPHOS) contributes to disease progression and therapeutic resistance in MCL. In this study, we

95 employed MCL cell lines as a model to investigate the role of ACSS1 in acetate metabolism under nutrient-
96 deprived conditions. Using extensive ^{13}C-acetate stable isotope tracing and genetic knockdown of ACSS1,
97 we uncover a previously unrecognized function of ACSS1 in supporting acetate-fueled survival and de
98 novo pyrimidine synthesis. These findings highlight ACSS1 as a critical mediator of metabolic adaptation
99 in aggressive, therapy-resistant MCL.
100
101 **Results**
102 **ACSS1 expression shows variable expression in MCL and DLBCL samples**
103 To validate ACSS1 protein expression in clinical samples, we performed immunohistochemistry (IHC) on
104 tumor tissue microarrays (TMAs) from mantle cell lymphoma (MCL) patient biopsies (n = 27) obtained
105 from Fox Chase Cancer Center. ACSS1 staining was detected in 92.6% of MCL cases (25/27), with
106 expression levels categorized as strong in 7 cases (25.9%), moderate in 9 cases (33.3%), and weak in 9
107 cases (33.3%) (Fig. 1A, B). A representative low-magnification image of the TMA block is shown in
108 Supplementary Fig. 1A. In chronic lymphocytic leukemia (CLL) patient samples (n = 13), IHC analysis
109 revealed ACSS1 expression in 7 cases (53.8%), as shown in Supplementary Fig. 1A. We next evaluated
110 diffuse large B-cell lymphoma (DLBCL) samples (n = 44). We observed ACSS1 positivity in 35 cases
111 (79.5%) (Fig. 1C), including strong expression in 6 cases (13.6%), moderate in 14 (31.8%), and weak in 15
112 (34.1%) (Fig. 1D). The corresponding TMA overview is provided in Supplementary Fig. 1B. These data
113 confirm frequent ACSS1 protein expression across multiple B-cell malignancies, consistent with
114 transcriptomic analyses.
115 To validate the specificity of the ACSS1 antibody for IHC staining, a breast cancer sample was tested using
116 immunofluorescence with ACSS1 and the mitochondrial marker VDAC1(Supplementary Fig. 2A).
117 Negative ACSS1 staining was noted (Supplementary Fig. 2B). To confirm ACSS1 expression in
118 mitochondria, we performed fractionation on MCL cell lines Maver and Jeko-1. Immunoblotting revealed
119 that ACSS1 is primarily located in mitochondria (Supplementary Fig. 2C).
120

121 To further investigate the ACSS1 expression in various cancer models, we analyzed publicly available
122 RNA-seq data from hematological malignancy cell lines using the Expression Atlas
123 (https://www.ebi.ac.uk/gxa/home). This analysis focused on hematopoietic and lymphoid-derived cancer
124 models, including mantle cell lymphoma (MCL), diffuse large B-cell lymphoma (DLBCL), chronic
125 lymphocytic leukemia (CLL), acute myeloid leukemia (AML), and anaplastic large cell lymphoma
126 (ALCL). Among acetyl-CoA synthetases, mitochondrial ACSS1 exhibited notably high expression in non-
127 Hodgkin lymphoma (NHL) cell lines and patient-derived samples. In contrast, ACSS3 expression was
128 negligible across all profiled lines (Supplementary Fig. 3A, B). To extend these observations, we examined
129 the expressions of ACSS1 and ACSS2 in hematopoietic and lymphoid malignancies using The Cancer
130 Genome Atlas (TCGA). ACSS1 was overexpressed in 36.2% of 221 hematopoietic and lymphoid samples,
131 with only 1.36% showing reduced expression (Table 1). Given the limited characterization of ACSS1 in
132 solid tumors, we further assessed its expression across multiple cancer types using TCGA. ACSS1 was
133 significantly overexpressed relative to matched normal tissue in several malignancies, including lung
134 (10.89%), ovarian (29.32%), prostate (16.47%), central nervous system (79.91%), cervical (84.04%), large
135 intestine (25.9%), and head and neck squamous cell carcinoma (24.71%) (Table 1). These findings suggest
136 that ACSS1 upregulation is a recurrent feature across both hematological and solid tumors, highlighting its
137 potential role in cancer-associated acetate metabolism.
138
139 **Acetate feeds the TCA cycle in MCL and DLBCL cells in an ACSS1-dependent manner**
140 Our analysis of patient-derived TMA, TCGA data, and hematological cancer cell lines revealed variable
141 ACSS1 expression across mantle cell lymphoma (MCL) and diffuse large B-cell lymphoma (DLBCL)
142 models. Notably, ACSS1 mRNA levels were low in MCL-RL cells but were significantly elevated in Jeko-
143 1 and Maver MCL cell lines, exhibiting 18-fold and 24-fold higher expression, respectively (Fig. 2A). In
144 contrast, ACSS2 expression remained low and was not differentially expressed across these MCL lines
145 (Fig. 2B). Similarly, high ACSS1 mRNA levels were observed in DLBCL cell lines, whereas one cell line
146 OCI-LY1 displayed low ACSS1 expression (Fig. 2C). Consistent with MCL, ACSS2 expression was

147 uniformly low in DLBCL lines (Fig. 2D). Immunoblot analysis of five MCL cell lines (Jeko-1, Maver,
148 Mino, Granta-519, and RL) confirmed robust ACSS1 protein expression in all except MCL-RL cells (Fig.
149 2E). Likewise, immunoblotting of four DLBCL cell lines demonstrated elevated ACSS1 protein levels in
150 all except OCI-LY1 cells (Fig. 2F). These findings suggest that ACSS1 expression correlates with variable
151 expressions in both MCL and DLBCL models.

152 To investigate the relationship between ACSS1 expression and acetate metabolism, we performed stable
153 isotope tracing using ^{13}C-labeled acetate, followed by liquid chromatography–mass spectrometry (LC-MS)
154 to analyze mass isotopologue distributions (MIDs) of tricarboxylic acid (TCA) cycle intermediates as
155 illustrated in schematics (Fig. 2G). Stable isotope tracing with ^{13}C-labeled acetate revealed distinct
156 differences in acetate utilization correlated with ACSS1 expression levels. Analysis of acetyl-CoA mass
157 isotopologue distributions showed significant variation in both unlabeled and labeled species among the
158 three MCL cell lines (Fig. 2H). To further assess the metabolic fate of acetate-derived carbon, we quantified
159 the incorporation of ^{13}C into tricarboxylic acid (TCA) cycle intermediates, including citrate, α-ketoglutarate
160 (α-KG), succinate, and malate. Citrate labeling patterns differed markedly among RL, Jeko-1, and Maver
161 cells increased ^{13}C-acetate derived labeling ($p < 0.0001$) (Fig. 2I). Similarly, α-KG showed significant
162 differences in M+2, M+3, M+4, and M+5 isotopologues, particularly between Jeko-1/Maver and the low-
163 ACSS1 RL cells (Fig. 2J). These trends were also observed in succinate (Fig. 2K) and malate (Fig. 2L),
164 with higher ^{13}C incorporation in Jeko-1 and Maver relative to RL. Collectively, these findings indicate that
165 elevated ACSS1 expression enhances acetate utilization and contributes to increased TCA cycle flux in
166 MCL cell lines.

167 To elucidate the role of ACSS1 in mitochondrial acetate metabolism, we silenced ACSS1 in two MCL cell
168 lines, Jeko-1 and Maver, which exhibit high endogenous ACSS1 expression. Knockdown efficiency was
169 confirmed at the transcript and protein levels using quantitative PCR and immunoblotting, respectively
170 (Fig. 2M, N). To determine whether ACSS1 drives mitochondrial acetate metabolism, we conducted ^{13}C-
171 acetate labeling analysis in both shControl and ACSS1 knockdown (shACSS1) cell lines, as illustrated in
172 the schematic (Fig. 2O). Given that most mammalian cells rely primarily on glucose and glutamine for

173 energy production, we hypothesized that ACSS1 is particularly critical under nutrient-deprived conditions.
174 Cells were cultured for 24 hours in ^{13}C-acetate–supplemented RPMI medium lacking glucose and
175 glutamine, with 1% dialyzed FBS. Metabolomic analysis revealed a significant reduction in acetyl-CoA
176 labeling in ACSS1 knockdown Jeko-1 cells $p < 0.0001$(Fig. 2P). To distinguish between cytosolic and
177 mitochondrial acetyl-CoA pools, we quantified mitochondrial acetylcarnitine labeling. ACSS1 knockdown
178 led to a marked reduction in acetylcarnitine M+2 labeling in both Jeko-1 (>40%; $p < 0.0003$) and Maver (
179 $p < 0.0005$) cells (Fig. 2Q), supporting a key role for ACSS1 in mitochondrial acetate utilization. Further
180 analysis of ^{13}C-acetate–derived MIDs in TCA cycle intermediates demonstrated that ACSS1 knockdown
181 decreased citrate M+2–M+5 labeling in both cell lines, consistent with reduced carbon entry from acetate
182 through multiple TCA cycle turns (Fig. 2R). Additional intermediates including aconitate, α-ketoglutarate,
183 and malate exhibited similar reductions in ^{13}C labeling upon ACSS1 silencing (Fig. 2S-U). These results
184 collectively indicate that ACSS1 is essential for converting acetate into mitochondrial acetyl-CoA, fueling
185 oxidative phosphorylation via the TCA cycle, particularly under nutrient-limited conditions. Thus, ACSS1
186 supports mitochondrial bioenergetics in MCL cells with elevated ACSS1 expression.
187 Building on the observed role of ACSS1 in mitochondrial acetate metabolism and its influence on TCA
188 cycle activity, we hypothesized that ACSS1 also modulates oxidative phosphorylation (OXPHOS) through
189 regulation of oxygen consumption rate (OCR). To evaluate this, we measured basal OCR in glucose-starved
190 RL (low ACSS1-expressing), Jeko-1, and Maver (high ACSS1-expressing) MCL cell lines following
191 exposure to 1 mM acetate. Acetate supplementation led to a significant increase in OCR in Jeko-1 (24%, P
192 < 0.002) and Maver (30%, $P < 0.0001$) cells. In contrast, RL cells exhibited minimal response (Fig. 2V).
193 These findings suggest that ACSS1 expression enables acetate-fueled mitochondrial respiration under
194 glucose-limiting conditions. To further confirm the role of ACSS1 in regulating acetate-dependent
195 OXPHOS, we compared OCR in control (shCon) and ACSS1 knockdown (shACSS1) Jeko-1 and Maver
196 cells. In both cell lines, ACSS1 silencing resulted in a marked reduction in basal and stress-induced OCR
197 compared to control cells (Fig. 2W, X), indicating that ACSS1 is critical for sustaining mitochondrial

198 respiration in the presence of acetate. Collectively, these results underscore the importance of ACSS1 in
199 driving acetate-supported oxidative metabolism in MCL cells.
200
201 **ACSS1 supports pyrimidine metabolism**
202 Based on the differential expression of ACSS1 in MCL cell lines high in Jeko-1 and Maver, and low in RL
203 we aimed to investigate ACSS1's role in acetate metabolism under nutrient-deprived conditions. To do this,
204 we performed ^{13}C-acetate tracing in these cell lines. Our metabolic analysis, which examined changes in
205 steady-state metabolite pathways and enrichment patterns, revealed perturbations in pyrimidine
206 biosynthesis pathways. To determine whether acetate directly contributes to pyrimidine biosynthesis, we
207 analyzed the incorporation of ^{13}C into key metabolic precursors, as illustrated in the schematic (Fig. 3A).
208 In Jeko-1 and Maver cells, which express high levels of ACSS1, we observed a significant increase in ^{13}C-
209 acetate–derived M+2 to M+5 labeling of aspartate and glutamate two critical intermediates for de novo
210 pyrimidine synthesis compared to low-ACSS1-expressing RL cells ($P < 0.0001$, Fig. 3B, C). These findings
211 indicate that ACSS1 enhances pyrimidine biosynthesis by supporting the generation of TCA cycle–derived
212 intermediates under acetate-reliant, nutrient-limited conditions. To further evaluate acetate's contribution
213 to pyrimidine synthesis, we examined the labeling patterns in downstream intermediates. Isotope tracing
214 revealed a significant enrichment of M+2 to M+5 ^{13}C-labeled orotate, UMP, UDP, and CDP in Jeko-1 and
215 Maver cells compared to RL ($P < 0.0001$, Fig. 4D–G), further supporting a model in which ACSS1 drives
216 acetate-dependent pyrimidine biosynthesis.
217 Next, we hypothesized that overexpression of ACSS1 in Jeko-1 and Maver cell lines drives acetate
218 metabolism in MCL. To investigate this, we silenced ACSS1 expression in both cell lines using lentiviral
219 short hairpin RNA (shRNA) targeting ACSS1. The resulting shACSS1 and shCon cell lines were
220 subsequently used in ^{13}C-acetate tracing experiments to assess alterations in acetate metabolism. Our
221 metabolomics analysis data showed a highly significant reduction in M+2 to M+5 ^{13}C-labeling of aspartate
222 and glutamate in shACSS1 Jeko-1 and Maver cells compared to shCon ($P < 0.0001$, Fig. 3H, I). Next, ^{13}C-
223 acetate isotope tracing revealed a significant reduction in M+2 to M+5 ^{13}C-labeled dihydroorotate and

224 orotate in shACSS1 Jeko-1 and Maver cells compared to scramble controls ($P < 0.0001$, Fig. 3J, K).
225 Comparative analysis of shACSS1 and shCon Jeko-1 and Maver cells cultured with ^{13}C-acetate revealed
226 significant alterations in cellular metabolism. Of the 206 metabolites analyzed, 46 metabolites were
227 significantly changed (absolute fold change >1.5, $P < 0.05$), with the majority associated with the
228 pyrimidine synthesis pathway (Supplementary Fig. 4A, B). A subset of altered pyrimidine metabolites from
229 Jeko-1 cells is highlighted in Fig. 3L. Additionally, pathway and enrichment analyses confirmed the
230 enrichment of metabolites linked to pyrimidine biosynthesis (Fig. 3M, N). These findings suggest that
231 ACSS1 plays a critical role in channeling acetate-derived carbon into TCA cycle intermediates that support
232 de novo pyrimidine synthesis.
233 We hypothesized that silencing ACSS1 in Jeko-1 cells would impact the expression of key enzymes
234 involved in pyrimidine biosynthesis, as illustrated in the schematic (Fig. 3O). To test this, we isolated RNA
235 from shCon and shACSS1 cells cultured in complete media and performed quantitative RT-PCR to assess
236 the expression of CAD and DHODH. The results demonstrated altered expression of both genes in
237 shACSS1 cells compared to shCon (Fig. 3P). To further evaluate these findings at the protein level, we
238 conducted Western blot analysis under different nutrient conditions. Notably, shACSS1 cells exhibited
239 reduced CAD protein expression when cultured in acetate/glutamine-only media, whereas shCon cells
240 maintained stable CAD levels (Fig. 3Q).
241
242 **ACSS1 supports growth under nutrient restriction**
243 We confirmed efficient ACSS1 knockdown (KD) in Maver and Jeko-1 cells using Western blot analysis,
244 with two of four shRNA clones achieving near-complete protein depletion (Fig. 4A). ACSS1 KD led to a
245 significant reduction in cell growth ($P < 0.0001$), as assessed by automated cell counting and trypan blue
246 exclusion (Fig. 4B). To assess the role of ACSS2, Jeko-1 and Maver cells were treated with an ACSS2
247 inhibitor (10–30 μM), resulting in a dose-dependent decrease in cell growth (Fig. 4C). Under metabolic
248 stress conditions, cells were cultured in glucose- and glutamine-free media supplemented with 1% dialyzed
249 FBS. While the viability of shCon and shACSS1 cells remained stable in complete media, ACSS1 KD cells

250 showed a marked decline in viability under nutrient deprivation. Supplementation with 100 μM acetate
251 significantly rescued viability in ACSS1 KD cells (from 16% to >68%) and in controls (from 36% to
252 >82%), highlighting ACSS1's critical role in acetate metabolism (Fig. 4D, E). Although glucose and
253 glutamine supplementation restored viability in control cells, glutamine was less effective in rescuing
254 ACSS1 KD cells. To determine whether impaired pyrimidine synthesis contributed to cell death, we
255 supplemented cultures with 100 μM uridine under nutrient-deprived conditions. Uridine markedly
256 enhanced viability in both control and ACSS1 KD cells ($P < 0.0001$; Fig. 4F, G). A schematic model (Fig.
257 4H, I) summarizes these findings, illustrating how ACSS1 supports TCA cycle intermediates and
258 pyrimidine precursor production, and identifying potential therapeutic vulnerabilities associated with
259 ACSS1 loss.
260

261 **Discussion**

262 In this study, we identify ACSS1 as a key metabolic enzyme that enables mantle cell lymphoma (MCL)
263 cells to utilize acetate as a carbon source under nutrient-limited conditions. By integrating TCGA analysis,
264 ^{13}C-acetate isotope tracing metabolomics, and functional assays, we show that ACSS1 is highly expressed
265 in MCL and other hematological malignancies and contributes to metabolic flexibility by supporting
266 mitochondrial acetate metabolism, particularly when glucose and glutamine are scarce.
267 Our data show that MCL cell lines with high ACSS1 expression, such as Jeko-1 and Maver, demonstrate
268 increased incorporation of ^{13}C-acetate into TCA cycle intermediates, pyrimidine precursors, and
269 downstream nucleotides, compared to RL cells with low ACSS1 expression cells. This suggests a model in
270 which ACSS1 acts as a mitochondrial gatekeeper for acetate utilization, enabling continued energy
271 production and biosynthesis in adverse nutrient environments. These findings are in agreement with prior
272 studies in AML and melanoma models, where ACSS1 overexpression was linked to increased
273 mitochondrial incorporation of acetate-derived carbon into the TCA cycle(23).
274 Our immunohistochemical analysis of patient-derived tumor samples confirms that ACSS1 is frequently
275 expressed in MCL and DLBCL tissues, consistent with publicly available RNA-seq datasets from

276 hematologic and solid tumors. Notably, we observed heterogeneous ACSS1 expression within and across
277 lymphoma subtypes, suggesting metabolic diversity and differential reliance on acetate metabolism in the
278 tumor microenvironment. ACSS1 expression correlated with increased incorporation of ^{13}C-labeled acetate
279 into TCA cycle intermediates and pyrimidine pathway metabolites, highlighting its role in maintaining
280 biosynthetic capacity under conditions of glucose and glutamine deprivation.
281 Importantly, inhibiting ACSS1 impairs this metabolic flexibility. Our results show that knocking down
282 ACSS1 markedly decreases ^{13}C-acetate integration into TCA cycle intermediates, dihydroorotate, and
283 orotate, which results in reduced pyrimidine production and diminished cell viability when nutrients are
284 limited. These effects were partly restored by adding exogenous acetate or uridine, confirming that ACSS1
285 supports nucleotide synthesis through mitochondrial acetate metabolism. Additionally, oxygen
286 consumption rates (OCR) depend on ACSS1 expression, showing that acetate oxidation via ACSS1
287 contributes to mitochondrial respiration and energy generation. Overall, our results identify ACSS1 as a
288 key regulator of mitochondrial acetate metabolism in MCL. Unlike the better-understood cytosolic enzyme
289 ACSS2, which promotes lipid biosynthesis and histone acetylation(24-26). ACSS1 specifically directs
290 acetate into mitochondrial oxidative pathways and biosynthesis(14). In earlier report on the role
291 Mitochondrial ACSS1-K635 acetylation knock-in mice shows altered liver lipid metabolism on a ketogenic
292 diet(27). In other report ACSS1-K635 acetylation knock-in mice exhibit altered metabolism, cell
293 senescence, and nonalcoholic fatty liver disease(3). This highlights the significance of compartmentalized
294 acetate metabolism in helping cancer cells survive under metabolic stress.
295 Therapeutically, these findings open new avenues for targeting metabolic dependencies in MCL. Inhibiting
296 acetate metabolism, either through direct ACSS1 inhibition or limiting acetate availability, may hinder
297 tumor cell survival, especially in nutrient-poor microenvironments like the tumor core or during treatment-
298 induced metabolic stress. Additionally, ACSS1 expression could serve as a biomarker to stratify tumors
299 based on their dependence on mitochondrial acetate metabolism. Our results also suggest potential
300 therapeutic implications. Tumors with high ACSS1 expression may be selectively vulnerable to strategies
301 that disrupt acetate metabolism or target downstream biosynthetic pathways such as pyrimidine synthesis.

302 In summary, we provide evidence that ACSS1-driven acetate utilization supports pyrimidine biosynthesis
303 and cell survival in MCL cells under metabolic stress. These findings advance our understanding of
304 metabolic plasticity in lymphoid malignancies and highlight ACSS1 as a potential metabolic vulnerability
305 with therapeutic relevance.
306

307 **Materials and Methods**

308 ACSS1 (Cat#17138-1-AP,RRID:AB_2289182), ACLY (Cat# 67166-1-Ig; RRID:AB_2882462), GAPDH
309 (Cat# 60004-1-Ig;RRID:AB_2107436), DHODH (Cat# 14877-1-AP, RRID:AB_2091723), CAD (Cat#
310 16617-1-AP, RRID:AB_2878289) and VDAC1 (Cat# 66345-1-Ig, RRID:AB_2881725) from Proteintech
311 Inc., ACSS2 (Cat#3658S; RRID:AB_2222710) from Cell Signaling Technology. ^{13}C2-Sodium acetate
312 (Cat#CLM-440-1) from Cambridge Isotope Laboratories. The special media, D-Glucose-free RPMI 1640
313 (REF 11879-020), was obtained from Gibco. RPMI 1640 (-) Glutamine free and (-) D-Glucose free media
314 were obtained from BI, Biological Industries, Israel Beit-Haemek. Uridine (Sigma, catalog#U3750-1G).
315

316 **MCL and DLBCL cell lines**

317 Cell lines from different lymphomas were used, including MCL-RL(28), a cell line derived from a patient
318 with MCL at the University of Pennsylvania, Philadelphia, PA, JeKo-1, Maver, Rec-1, and Granta519 for
319 MCL; OCI-LY1, OCI-LY4, OCI-LY8, and TOLEDO for DLBCL; All commercially available cell lines
320 were obtained from the American Type Culture Collection (ATCC). All the cell lines were regularly tested
321 for Mycoplasma contamination using Mycoplasma detection kits from Thermo Fisher Scientific and
322 authenticated. All cells were grown in RPMI medium supplemented with 10% FBS and 1%
323 penicillin/streptomycin under a humidified 37°C/5% CO_2 incubator. The cell lines are validated for
324 authenticity and routinely tested for mycoplasma contamination.

325 **Nutrient starvation in cell culture**

326 For nutrient-deprivation experiments, cells were washed once with phosphate-buffered saline. The
327 glutamine-free medium was made with RPMI devoid of glutamine and glucose and retained the same
328 nutrient concentrations as standard RPMI with dialyzed 10% FBS and 25 mM Glucose. A glucose-free
329 medium was made with RPMI devoid of glutamine and glucose and retained the same nutrient
330 concentrations as standard RPMI with dialyzed 10% FBS and 2 mM Glutamine. Complete RPMI was
331 prepared by supplementing with 2 mM L-Glutamine and 25 mM Glucose to RPMI devoid of glutamine and
332 glucose. For acetate supplementation, Sodium acetate at a final concentration of 5 mM was supplemented
333 to Glutamine-free or Glucose-free media or both Glutamine/Glucose-free media.

334 **ACSS1 and mitochondrial fractionation**

335 For mitochondria isolation, $50x10^6$ cells of Jeko-1 and Maver cell lines were harvested, and mitochondria
336 were isolated according to the instructions of the product manual (catalog # 89874, Thermofisher). The
337 protein estimation was measured, and an equal amount of protein was separated on a 10% NuPAGE gel
338 and processed for western blotting as described below.

339 **ACSS1 knockdown (KD) in MCL cell lines**

340 Jeko-1 and Maver cell lines were transduced with the scramble PLKO.1-PURO NON-TARGET
341 CONTROL (SHC016V-1EA) and ACSS1 shRNA, TRCN0000436733, TRCN0000045380,
342 TRCN0000045381, TRCN0000424197 and TRCN0000423168 all purchased from Millepore-Sigma-
343 Aldrich. The ready-to-transduce lentivirus particles were directly mixed with 100,000 cells (Jeko-1 and
344 Maver) in the presence of polybrene (catalog#TR-1003-G, Millepore Sigma) in a 96-well plate. The media
345 was replaced with fresh RPMI after 16 hours of incubation. The cells were cultured for an additional 3 days
346 and then selected with puromycin.

347 **Western blotting**

348 Cells were harvested and processed for western blotting as previously described with respective antibodies;
349 blots were developed using the Ibright 1500 imaging system (Thermo Scientific)(29).

350 **Reverse transcription quantitative polymerase chain reaction**

351 MCL-RL, Jeko-1, and Maver, along with Jeko-1 shCon or shACSS1 cells, were seeded in six-well plates
352 up to 48 hours. RNA isolation and DNase treatment were performed according to the kit protocol (Qiagen
353 #74104, #79254). The RNA concentration was measured, and 1 µg was used for cDNA synthesis, which
354 was conducted using the SuperScript IV (Invitrogen #18091050). For the quantitative reverse transcription
355 polymerase chain reaction (qRT-PCR), 1 µL of cDNA was utilized. Each reaction contained: 1 µL of cDNA,
356 5 µL of SYBR Green mix (Applied Biosystem, A25742), 0.5 µL of forward primer (from a 10 mM stock),
357 0.5 µL of reverse primer (from a 10 mM stock), and 3 µL of dH2O. Each condition was tested in technical
358 triplicate. Primers used are as follows,

359 **Primer Sequence 5' to 3'**

360 ACSS1, Forward- TTG AGA GCA CCC CAG TTT ATC; Reverse- GCA TCA CCG TAT TTC AGC AAC
361 ACSS2, Forward- GGA TCA CTG GTC ATT CCT AC; Reverse- GTG CTG TGT AGA ACT TGG TC
362 CAD, Forward- AGT GGT GTT TCA AAC CGG CAT; Reverse- CAG AGG ATA GGT GAG CAC TAA
363 GA and DHODH, Forward-CCACGGGAGATGAGCGTTTC; Reverse-CAGGGAGGTGAAGCGAACA

364 **Immunohistochemistry (IHC) of MCL, DLBCL, and CLL patient-derived biopsy samples.**

365 We followed the protocols approved by the Institutional Review Board (IRB) of Fox Chase Cancer Center.
366 Frozen DLBCL and MCL patient tissue samples were isolated from IRB-exempt discarded specimens of
367 patients with diffuse large B-cell lymphoma (DLBCL) obtained through the Fox Chase Cancer Center Bio
368 Specimen Repository. Human tissue microarrays for patients with MCL ($n = 22$), DLBCL ($n = 28$) and CLL
369 (n=7) were used to examine ACSS1. The expression of ACSS1 was analyzed according to the pathology
370 grade of the samples. Tissues were collected and fixed in 10% phosphate-buffered formaldehyde (formalin)
371 for 24-48 hrs, dehydrated and embedded in paraffin. Hematoxylin and eosin (H&E) stained sections were
372 used for morphological evaluation and unstained sections for IHC studies. IHC staining was performed on
373 a VENTANA Discovery XT automated staining instrument (Ventana Medical Systems) using VENTANA
374 reagents according to the manufacturer's instructions. Slides were de-paraffinized using EZ Prep solution
375 (cat # 950–102) for 16 min at 72 °C. Epitope retrieval was accomplished with CC1 solution (cat # 950–
376 224) at high temperature (eg, 95–100 °C) for 32 min. Rabbit primary antibodies (ACSS1: 1:200, ACSS1

377 (Cat#17138-1-AP, RRID :AB_2289182) were tittered with a TBS antibody diluent into user-fillable
378 dispensers for use on the automated stainer. Immune complex was detected using the Ventana OmniMap
379 anti-rabbit detection kit (760-4311) and developed using the VENTANA ChromMap DAB detection kit
380 (cat # 760-159) according to the manufacturer's instructions. Slides were then counterstained with
381 hematoxylin II (cat # 790-2208) for 8 min, followed by Bluing reagent (cat # 760-2037) for 4 min. The
382 slides were dehydrated with ethanol series, cleared in xylene, and mounted. As a negative control, the
383 primary antibody was replaced with normal rabbit IgG to confirm the absence of specific staining. Stained
384 slides were scanned using an Aperio ScanScope CS 5 slide scanner (Aperio, Vista, CA, USA). Scanned
385 images were then viewed and captured with Aperio's image viewer software (ImageScope, version
386 11.1.2.760, Aperio).

387 **Cell proliferation and cell death analysis**

388 For measuring cell proliferation, MCL Jeko-1 and Maver parental cell lines were seeded at a density of 2 ×
389 10^4 cells per well in 96-well plates (Corning, NY, USA). Afterwards, the cells were treated with different
390 concentrations of the ACSS2 inhibitor and incubated for 72 hours. After incubation, the cells were counted
391 using the trypan blue method with a hemocytometer.

392 **Cell Culture Conditions under Nutrient Deprivation**

393 Jeko-1 and Maver lymphoma cell lines shCon and shACSS1 were cultured under various nutrient
394 conditions to assess the role of ACSS1 in supporting cell viability during metabolic stress.

395 Cells were seeded at a density of 2×10^5 cells/mL and cultured for 72 hours under the following conditions:
396 Complete RPMI medium supplemented with 10% FBS, Glucose- and glutamine-free RPMI supplemented
397 with 1% dialyzed FBS, Glucose- and glutamine-free RPMI supplemented with 1% dialyzed FBS and 1 mM
398 sodium acetate, Glucose- and glutamine-free RPMI supplemented with 1% dialyzed FBS and 2 mM
399 glucose, and Glucose- and glutamine-free RPMI supplemented with 1% dialyzed FBS and 2 mM glutamine
400 For pyrimidine depletion and rescue experiments, shACSS1 and shCon cells were cultured in glucose- and
401 glutamine-free RPMI supplemented with 1% dialyzed FBS, in the presence or absence of 100 μM uridine
402 (Cat# U3750-1G, Sigma-Aldrich), a pyrimidine nucleoside metabolite.

403 Following incubation, cell viability was assessed using the protocol as described in the kit for Annexin V /
404 Propidium Iodide (PI) Staining ((BD Biosciences Cat# 556547, RRID:AB_2869082BD) and flow
405 cytometry for cell viability assay.
406
407 **Metabolomics analysis**
408 Metabolomics analyses were conducted at The Wistar Institute Proteomics and Metabolomics Shared
409 Resource with slight modifications as previously described(30). For $^{13}C_2$-acetate tracing experiments, the
410 cells were cultured in glucose- and glutamine-free RPMI-1640 media supplemented with 500 µM labeled
411 $^{13}C_2$-acetate (Cambridge Isotope Laboratories Inc.), 10 mM unlabeled Glucose for 16 hours in triplicate.
412 The cells were counted using the trypan blue method, and an equal number of cells ($10x10^6$ cells/condition)
413 were spun down at 1,000 rpm for 5 minutes. The cell pellet was washed with cold PBS and snap-frozen in
414 liquid nitrogen. Unlabeled controls were generated for each cell line condition.
415 **Oxygen consumption rate (OCR) measurement by Seahorse analysis.**
416 The MCL cell lines (Jeko-1 shControl (control), Jeko-1 shACSS1 knockdown (KD), Maver shControl
417 (control), Maver shACSS1 knockdown (KD) were exposed to either -glucose (Glc) or 2 mM acetate (ACE)
418 for 1 hour and then thoroughly examined for mitochondrial respiration using the Seahorse-based method.
419 The XF Mitochondrial stress test kit protocols (Agilent) were followed using the Agilent Seahorse XFe96
420 analyzer per the manufacturer's instructions. In brief, cells were seeded in Seahorse XF 96-well plates at a
421 density of $1.2x\ 10^5$ cells per well with Assay Base media, supplemented with 10 mM Glucose, 1 mM
422 Sodium Pyruvate, and 2 mM Glutamine. The cell cultures were allowed to equilibrate for 1 hour at 37 °C
423 in a no-CO2 incubator. The Oxygen Consumption Rate was analyzed under basal conditions and after
424 treatment with different drugs, including 1 µM oligomycin A, 2 µM FCCP, and 0.5 µM Rot/AA. After the
425 analysis, the medium was removed, and the cells were suspended in RIPA lysis buffer. The protein content
426 of the cell lysates was then measured using the Bradford assay and used to normalize the respiratory
427 parameters. Samples were analyzed with at least 6 technical replicates. The data were assessed using XF
428 Wave Software (Seahorse Bioscience, Agilent).

429 **Statistics and reproducibility**

430 The student's unpaired t-test was used to analyze differences in quantitative (q)-PCR expression analysis,
431 and isotope-labeled metabolites compared with MCL-RL cell line vs. Jeko-1 and Maver in three ^{13}C-isotope
432 tracing experiments. For ACSS1 knockdown (KD) studies in Jeko-1 and Maver cell lines, an unpaired t-
433 test was used to analyze differences between control vs. KD cells ^{13}C-acetate isotope-labeled
434 metabolites. *P* values equal to or less than 0.05 were considered statistically significant without being
435 adjusted for multiple comparisons.

436

437

438 **References**

439 1. Hosios AM, Hecht VC, Danai LV, Johnson MO, Rathmell JC, Steinhauser ML, et al. Amino Acids
440 Rather than Glucose Account for the Majority of Cell Mass in Proliferating Mammalian Cells. Dev Cell.
441 2016;36(5):540-9.
442 2. Schug ZT, Vande Voorde J, Gottlieb E. The metabolic fate of acetate in cancer. Nat Rev Cancer.
443 2016;16(11):708-17.
444 3. Xu G, Quan S, Schell J, Gao Y, Varmazyad M, Sreenivas P, et al. Mitochondrial ACSS1-K635
445 acetylation knock-in mice exhibit altered metabolism, cell senescence, and nonalcoholic fatty liver
446 disease. Sci Adv. 2024;10(20):eadj5942.
447 4. Wang J, Yang Y, Shao F, Meng Y, Guo D, He J, et al. Acetate reprogrammes tumour metabolism
448 and promotes PD-L1 expression and immune evasion by upregulating c-Myc. Nat Metab. 2024.
449 5. Schwer B, Bunkenborg J, Verdin RO, Andersen JS, Verdin E. Reversible lysine acetylation controls
450 the activity of the mitochondrial enzyme acetyl-CoA synthetase 2. P Natl Acad Sci USA.
451 2006;103(27):10224-9.
452 6. Berg P. Acyl adenylates; an enzymatic mechanism of acetate activation. J Biol Chem.
453 1956;222(2):991-1013.
454 7. Comerford SA, Huang Z, Du X, Wang Y, Cai L, Witkiewicz AK, et al. Acetate dependence of
455 tumors. Cell. 2014;159(7):1591-602.
456 8. Bulusu V, Tumanov S, Michalopoulou E, van den Broek NJ, MacKay G, Nixon C, et al. Acetate
457 Recapturing by Nuclear Acetyl-CoA Synthetase 2 Prevents Loss of Histone Acetylation during Oxygen and
458 Serum Limitation. Cell Rep. 2017;18(3):647-58.
459 9. Wellen KE, Thompson CB. A two-way street: reciprocal regulation of metabolism and signalling.
460 Nat Rev Mol Cell Bio. 2012;13(4):270-U1.
461 10. Watkins PA, Maiguel D, Jia ZZ, Pevsner J. Evidence for 26 distinct acyl-coenzyme A synthetase
462 genes in the human genome. J Lipid Res. 2007;48(12):2736-50.
463 11. Murthy D, Attri KS, Shukla SK, Thakur R, Chaika NV, He CB, et al. Cancer-associated fibroblast-
464 derived acetate promotes pancreatic cancer development by altering polyamine metabolism via the
465 ACSS2-SP1-SAT1 axis. Nat Cell Biol. 2024.
466 12. Yun M, Bang SH, Kim JW, Park JY, Kim KS, Lee JD. The importance of acetyl coenzyme A
467 synthetase for 11C-acetate uptake and cell survival in hepatocellular carcinoma. J Nucl Med.
468 2009;50(8):1222-8.

13. Comerford SA, Huang Z, Du X, Wang Y, Cai L, Witkiewicz AK, et al. Acetate Dependence of Tumors. Cell. 2014;159(7):1591-602.
14. Mashimo T, Pichumani K, Vemireddy V, Hatanpaa KJ, Singh DK, Sirasanagandla S, et al. Acetate Is a Bioenergetic Substrate for Human Glioblastoma and Brain Metastases. Cell. 2014;159(7):1603-14.
15. Schug ZT, Peck B, Jones DT, Zhang QF, Grosskurth S, Alam IS, et al. Acetyl-CoA Synthetase 2 Promotes Acetate Utilization and Maintains Cancer Cell Growth under Metabolic Stress. Cancer Cell. 2015;27(1):57-71.
16. Lee MY, Yeon A, Shahid M, Cho E, Sairam V, Figlin R, et al. Reprogrammed lipid metabolism in bladder cancer with cisplatin resistance. Oncotarget. 2018;9(17):13231-43.
17. Li CJ, Chiu YH, Chang C, Chang YCI, Sheu JJC, Chiang AJ. Acetyl Coenzyme A Synthase 2 Acts as a Prognostic Biomarker Associated with Immune Infiltration in Cervical Squamous Cell Carcinoma. Cancers. 2021;13(13).
18. Sakakibara I, Fujino T, Ishii M, Tanaka T, Shimosawa T, Miura S, et al. Fasting-induced Hypothermia and Reduced Energy Production in Mice Lacking Acetyl-CoA Synthetase 2. Cell Metab. 2009;9(2):191-202.
19. Calhoun S, Duan L, Maki CG. Acetyl-CoA synthetases ACSS1 and ACSS2 are 4-hydroxytamoxifen responsive factors that promote survival in tamoxifen treated and estrogen deprived cells. Transl Oncol. 2022;19.
20. Aitken SC, Lippman ME. Hormonal-Regulation of De Novo Pyrimidine Synthesis and Utilization in Human-Breast Cancer-Cells in Tissue-Culture. Cancer Res. 1983;43(10):4681-90.
21. Kamphorst JJ, Chung MK, Fan J, Rabinowitz JD. Quantitative analysis of acetyl-CoA production in hypoxic cancer cells reveals substantial contribution from acetate. Cancer Metab. 2014;2:23.
22. Monga N, Tam C, Garside J, Davids MS, Ward K, Quigley J, et al. Clinical efficacy and safety of first-line treatments in patients with mantle cell lymphoma: A systematic literature review. Crit Rev Oncol Hematol. 2021;158:103212.
23. Hlavaty SI, Salcido KN, Pniewski KA, Mukha D, Ma W, Kannan T, et al. ACSS1-dependent acetate utilization rewires mitochondrial metabolism to support AML and melanoma tumor growth and metastasis. Cell Rep. 2024;43(12):114988.
24. Mews P, Donahue G, Drake AM, Luczak V, Abel T, Berger SL. Acetyl-CoA synthetase regulates histone acetylation and hippocampal memory. Nature. 2017;546(7658):381-6.
25. Hu W, Wang X, Fang Z, Zhang J, Tirumalasetty MB, Miao QR. High fructose promotes MYCN-amplified neuroblastoma progression through NgBR-ACSS2-mediated biosynthesis of acetyl-CoA. Cell Rep. 2025;44(7):115947.
26. Zhang Y, He S, Wang X, Wang X, He MY, Yu XX, et al. ACSS2 mediates an epigenetic pathway to regulate beta-cell adaptation during gestation in mice. Nat Commun. 2025;16(1):4697.
27. Xu G, Schell J, Quan S, Gao Y, Wei SJ, Pan M, et al. Mitochondrial ACSS1-K635 acetylation knock-in mice exhibit altered liver lipid metabolism on a ketogenic diet. Free Radic Biol Med. 2025;232:260-8.
28. Lee SC, Shestov AA, Guo LL, Zhang Q, Roman JC, Liu XB, et al. Metabolic Detection of Bruton's Tyrosine Kinase Inhibition in Mantle Cell Lymphoma Cells. Molecular Cancer Research. 2019;17(6):1365-77.
29. Basappa J, Citir M, Zhang Q, Wang HY, Liu XB, Melnikov O, et al. ACLY is the novel signaling target of PIP/PIPand Lyn in acute myeloid leukemia. Heliyon. 2020;6(5).
30. Di Marcantonio D, Martinez E, Kanefsky JS, Huhn JM, Gabbasov R, Gupta A, et al. ATF3 coordinates serine and nucleotide metabolism to drive cell cycle progression in acute myeloid leukemia. Mol Cell. 2021;81(13):2752-+.

Acknowledgments

We are grateful to Dr. Erica Golemis, Senior Associate Dean of Research at Lewis Katz School of Medicine, Temple University Health System, and Professor and Chair, Cancer and Cellular Biology, Fox Chase Cancer Center, Philadelphia, for critically reading the manuscript and providing feedback to improve the paper. We thank the IHC core facility members at Fox Chase Cancer Center for providing excellent IHC staining. We thank Dr. Andrey Efimov, Bio Imaging Facility, Fox Chase Cancer Center, for confocal imaging. We created the figures in this manuscript using the Biorender program..

Funding:

The funding for the startup comes from Fox Chase Cancer Center to MW. The Wistar Institute Proteomics and Metabolomics Shared Resource is supported by NIH Cancer Center Support Grant CA010815. The metabolomics analysis was performed on a Thermo Q-Exactive HF-X mass spectrometer purchased with NIH grant S10 OD023586.

Author Contributions:

Conceptualization: J.B. Writing—original draft: J.B. Data curation: J.B. Methodology: J.B., A.R.G. and N.V.S. Formal Analysis: J.B., A.R.G., and D.R. Investigation: J.B., C.L., S.W., D.R., O.M., N.V.S., V.S.M., P.J., M.E., R.N., and K.Q.C. Visualization: J.B., A.R.G., and C.L. Validation: J.B., A.R., D.R. and N.V.S. Resources: H.B., and K.E.W. Supervision: J.B. Writing—review and editing: J.B., A.R.G, C.L., K.E.W. and M.A.W. Funding acquisition: M.A.W. Read and approved of the manuscript: J.B., A.R.G., C.L., S.W., D.R., O.M., N.V.S., V.S.M., P.J., M.E., K.C., P.L., R.N., H.G., K.E.W., and M.A.W.

Competing interests

All authors declare that they have no competing interests.

Data and materials availability: All data needed to evaluate the conclusions in the paper are present in the paper and/or the Supplementary Materials.

542 **Table of Contents**

543 **Main Fig. 1-4**

544 **Supplementary Fig. 1-4**

545 Table 1

546

547 **Fig. 1**

548 **ACSS1 expression shows variable expression in MCL and DLBCL samples.**

549 **A,** Representative immunohistochemistry (IHC) images of ACSS1 protein expression in mantle cell
550 lymphoma (MCL) tissue microarray (TMA) cores, showing examples of strong, moderate, and weak
551 staining.

552 **B**, Quantification of ACSS1 IHC staining intensity in MCL (n = 27) samples. Staining intensity was
553 categorized as strong, moderate, weak, or negative.

554 **C,** Representative IHC images of ACSS1 expression in DLBCL TMA cores, corresponding to varying
555 expression levels.

556 **D,** Quantification of ACSS1 IHC staining intensity in diffuse large B-cell lymphoma (DLBCL, n = 44)
557 samples. Staining intensity was categorized as strong, moderate, weak, or negative.

558

559 Fig. 2

560 **Acetate feeds the TCA cycle in MCL and DLBCL cells in an ACSS1-dependent manner.**

561 **A-D**, Quantitative RT-PCR analysis of ACSS1 and ACSS2 mRNA expression in MCL (RL, Jeko-1, Maver)
562 and DLBCL (OCI-LY1, OCI-LY8) cell lines. ACSS1 is highly expressed in Jeko-1, Maver, and OCI-LY8,
563 while ACSS2 remains uniformly low.

564 **E, F**, Immunoblot analysis of ACSS1 protein levels across five MCL (e) and four DLBCL (f) cell lines
565 confirms elevated expression in all except RL and OCI-LY1, respectively. **G,** A schematic of ^{13}C-acetate
566 isotope tracing.

567 **H, I,** ^{13}C-acetate isotope tracing and LC-MS analysis of TCA cycle intermediates in RL, Jeko-1, and Maver
568 cells. unalabeled and labeled acetyl-CoA (**H**), M+0 to M+n isotopologues of citrate (**I**), α-ketoglutarate (**J**),
569 succinate (**K**), and malate (**L**) are enriched in ACSS1-high lines.

570 **M, N**, ACSS1 knockdown efficiency confirmed by qPCR and immunoblotting in Jeko-1 and Maver cells.
571 **O**, Schematic of isotope tracing strategy using ^{13}C-acetate in glucose- and glutamine-deprived media.

572 **P, Q**, ACSS1 knockdown reduces ^{13}C-acetate derived labeling of acetyl-CoA (**P**) and mitochondrial
573 acetylcarnitine (**Q**), confirming ACSS1's role in mitochondrial acetate conversion.

574 **R–U**, Stable isotope tracing reveals significantly decreased ^{13}C incorporation into citrate (**R**), aconitate (**S**),
575 α-ketoglutarate (**T**), and malate (**U**) upon ACSS1 silencing. **V**, Basal oxygen consumption rate (OCR)

576 increases in ACSS1-high Jeko-1 and Maver cells after acetate supplementation; no effect in low-ACSS1
577 RL cells.

578 **W, X**, ACSS1 knockdown reduces basal and stress-induced OCR in Jeko-1 (u) and Maver (v) cells under
579 acetate-reliant conditions.

580 All graphs show mean ± SD (n = 3 biological replicates), and all statistical analyses were conducted with
581 unpaired t-tests: $^{*}p < 0.05$, $^{**}p < 0.01$, $^{***}p < 0.001$, $^{****}p < 0.0001$

582 Fig.3

583 **ACSS1 supports pyrimidine metabolism.**

584 **A**, Schematic illustrating ^{13}C-acetate tracing strategy to assess incorporation into TCA cycle intermediates
585 and downstream pyrimidine biosynthesis.

586 **B, C**, Mass isotopologue distribution analysis of aspartate (**B**) and glutamate (**C**) in RL (low ACSS1),
587 Jeko-1, and Maver (high ACSS1) MCL cell lines shows significantly increased ^{13}C-labeling in ACSS1-
588 high cells under nutrient-limited conditions (RPMI lacking glucose/glutamine, supplemented with ^{13}C-
589 acetate).

590 **D–G**, Enhanced incorporation of ^{13}C into pyrimidine intermediates orotate (**D**), UMP (**E**), UDP (**F**), and
591 CDP (**G**) in Jeko-1 and Maver compared to RL cells, indicating acetate contribution to de novo
592 pyrimidine synthesis.

593 **H, I**, Knockdown of ACSS1 via shRNA (shACSS1) in Jeko-1 and Maver cells reduces ^{13}C-labeling of
594 aspartate (**H**) and glutamate (**I**) compared to scramble controls (shCon).

595 **J, K**, ^{13}C-labeling of dihydroorotate (**J**) and orotate (**K**) is also significantly decreased in shACSS1 cells,
596 confirming impaired pyrimidine biosynthesis.

597 **L**, Heat map highlighting significantly altered pyrimidine-related metabolites in Jeko-1 shACSS1 vs.
598 shCon cells (fold change >1.5, $P < 0.05$).

599 **M, N**, Metabolite enrichment and pathway analysis of 206 profiled metabolites in shACSS1 cells reveals
600 prominent suppression of the pyrimidine synthesis pathway.

601 **O**, Schematic of pyrimidine biosynthesis pathway showing ACSS1's proposed role and key enzymes
602 (CAD, DHODH).

603 **P**, qRT-PCR analysis of CAD and DHODH mRNA levels shows reduced expression in shACSS1 cells.

604 **Q**, Western blot analysis reveals decreased CAD protein expression in shACSS1 cells cultured in
605 acetate/glutamine-only media, supporting a regulatory role of ACSS1 in pyrimidine biosynthetic enzyme
606 expression under metabolic stress.

607 All graphs show mean ± SD (n = 3 biological replicates), and all statistical analyses were conducted with
608 unpaired t-tests: $^{*}p < 0.05$, $^{**}p < 0.01$, $^{***}p < 0.001$, $^{****}p < 0.0001$.

609 Fig. 4

610 **ACSS1 supports growth under nutrient restriction.**

611 **A**, Western blot analysis confirming efficient knockdown of ACSS1 in Maver and Jeko-1 cells using four
612 independent shRNA clones; two clones exhibited near-complete protein depletion.

613 **B**, ACSS1 knockdown (KD) significantly reduced cell growth, assessed by automated cell counting and
614 trypan blue exclusion over 72 hours ($P < 0.0001$).

615 **C**, Dose-dependent inhibition of cell growth by ACSS2 inhibitor (10–30 μM) in Jeko-1 and Maver cells
616 cultured under standard conditions.

617 **D, E**, Cell viability under metabolic stress (glucose/glutamine-free media + 1% dialyzed FBS) was
618 markedly reduced in shACSS1 cells compared to shCon. Supplementation with 100 μM acetate
619 significantly rescued viability in both groups, with a more pronounced effect in ACSS1 KD cells.

620 **F, G**, Supplementation with 100 μM uridine rescued viability in both control and ACSS1 KD cells under
621 nutrient-deprived conditions ($P < 0.0001$), implicating impaired pyrimidine biosynthesis in reduced cell
622 survival.

623 **H, I**, Schematic model depicting ACSS1-mediated conversion of acetate to mitochondrial acetyl-CoA,
624 feeding into the TCA cycle and supporting aspartate/glutamate production for pyrimidine biosynthesis.
625 The model highlights metabolic vulnerabilities upon ACSS1 depletion.

626 All graphs show mean ± SD (n = 3 biological replicates), and all statistical analyses were conducted with
627 unpaired t-tests: $^{*}p < 0.05$, $^{**}p < 0.01$, $^{***}p < 0.001$, $^{****}p < 0.0001$.

628

629

630

631 Supplementary Fig.1

632 **Overview of tissue microarrays (TMAs) and ACSS1 expression in lymphoma**.

633 **A**, Low-magnification overview of the mantle cell lymphoma (MCL) TMA block used for
634 immunohistochemical analysis of ACSS1 expression.

635 **B**, Representative IHC images showing ACSS1 staining in diffuse large B-cell lymphoma (DLBCL)
636 patient samples (n = 13). ACSS1 expression was detected in 7 cases (53.8%).

637

638 Supplementary Fig.2

639 **Validation of ACSS1 antibody specificity and mitochondrial localization**.

640 **A, B**, Immunofluorescence analysis of a breast cancer tissue section stained with antibodies against
641 ACSS1 (green) and the mitochondrial marker VDAC1 (red), with nuclei counterstained using DAPI
642 (blue). Confocal microscopy shows co-localization of ACSS1 and VDAC1 in positive control tissue.

643 **C**, Negative control showing absence of ACSS1 signal in breast cancer tissue, confirming antibody
644 specificity.

645 **D**, Subcellular fractionation and immunoblot analysis of MCL cell lines (Maver and Jeko-1) demonstrate
646 enrichment of ACSS1 in mitochondrial fractions. VDAC1 serves as a mitochondrial marker.

Supplementary Fig.3

ACSS1 is selectively expressed in non-Hodgkin lymphoma models.

A, RNA-seq–based expression analysis of acetyl-CoA synthetase family members (ACSS1, ACSS2, ACSS3) across hematological cancer cell lines using the Expression Atlas database. Data includes models of mantle cell lymphoma (MCL), diffuse large B-cell lymphoma (DLBCL), chronic lymphocytic leukemia (CLL), acute myeloid leukemia (AML), and anaplastic large cell lymphoma (ALCL).

B, ACSS1 expression is elevated in non-Hodgkin lymphoma (NHL) cell lines and patient-derived samples, whereas ACSS3 expression is consistently low or undetectable (FPKM <1) across all profiles.

Supplementary Fig. 4 |

ACSS1 knockdown alters pyrimidine-associated metabolites under acetate-reliant conditions.

A, B, Heatmap analysis of metabolomic profiling of shACSS1 and shControl Jeko-1 and Maver cells cultured in glucose- and glutamine-free media supplemented with 1% dialyzed FBS and ^{13}C-acetate. Of the 206 metabolites analyzed, 46 showed significant changes (fold change >1.5, $P < 0.05$), with a majority enriched in the pyrimidine biosynthesis pathway. Data represents results from two independent cell lines (Jeko-1 and Maver), each with triplicate biological replicates.

Table 1

Cancer type	Total number of samples tested	No. of samples over expressed	Over expressed (%)	No. of samples under expressed	Under expressed (%)
Hematologic and lymphoid	221	80	36.2	3	1.36
Central Nervous System	697	557	79.91	32	4.59
Lung	1019	111	10.89	None	None
Ovary	266	78	29.32	None	None
Cervix	307	258	84.04	29	9.45
Large Intestine	610	158	25.9	12	1.97
Prostate	498	82	16.47	3	0.6
Head and Neck	522	129	24.71	None	None

Fig.1

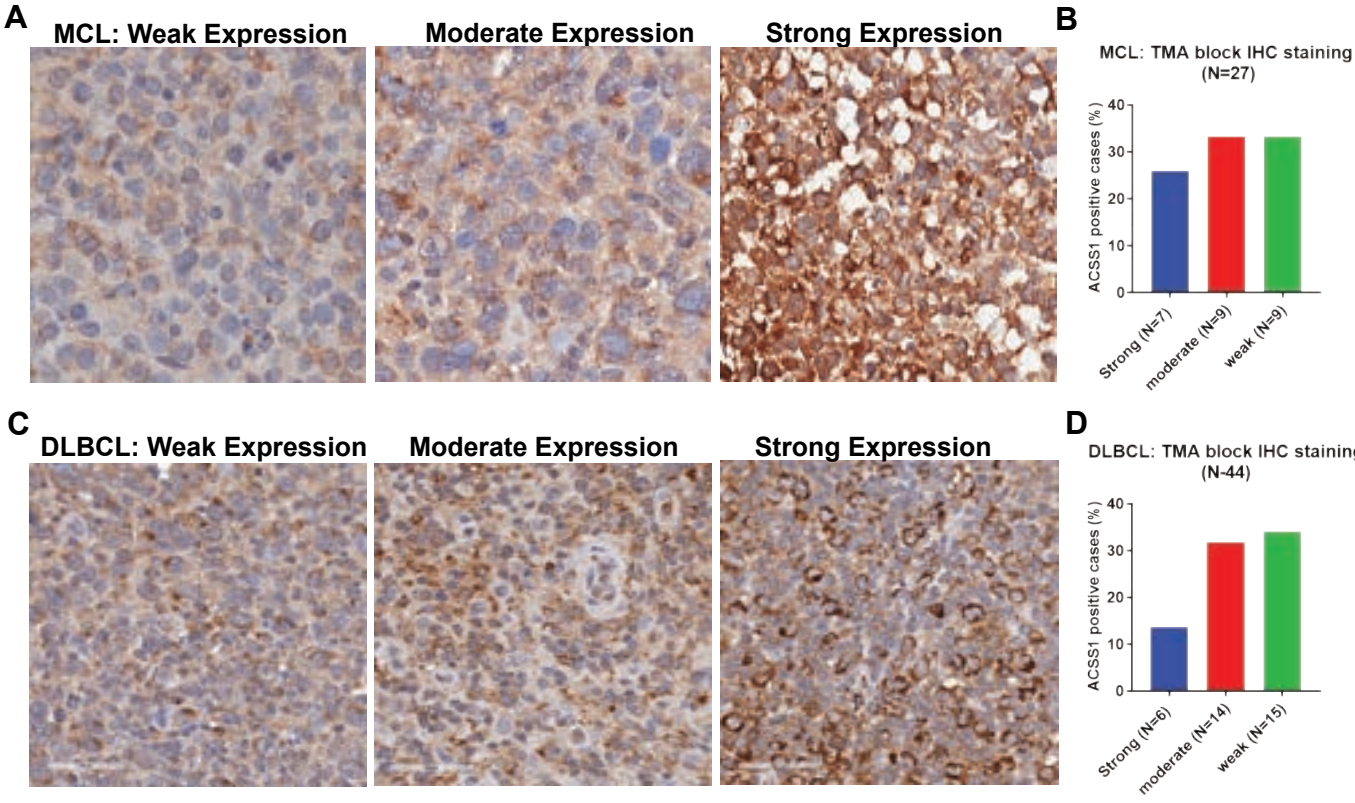
A
MCL: Weak Expression
Moderate Expression
Strong Expression
B
MCL: TMA block IHC staining
(N=27)
ACSS1 positive cases (%)
40
30
20
10
0
Strong (N=7)
moderate (N=9)
weak (N=9)
C
DLBCL: Weak Expression
Moderate Expression
Strong Expression
D
DLBCL: TMA block IHC staining
(N-44)
ACSS1 positive cases (%)
40
30
20
10
0
Strong (N=6)
moderate (N=14)
weak (N=15)

Fig.2

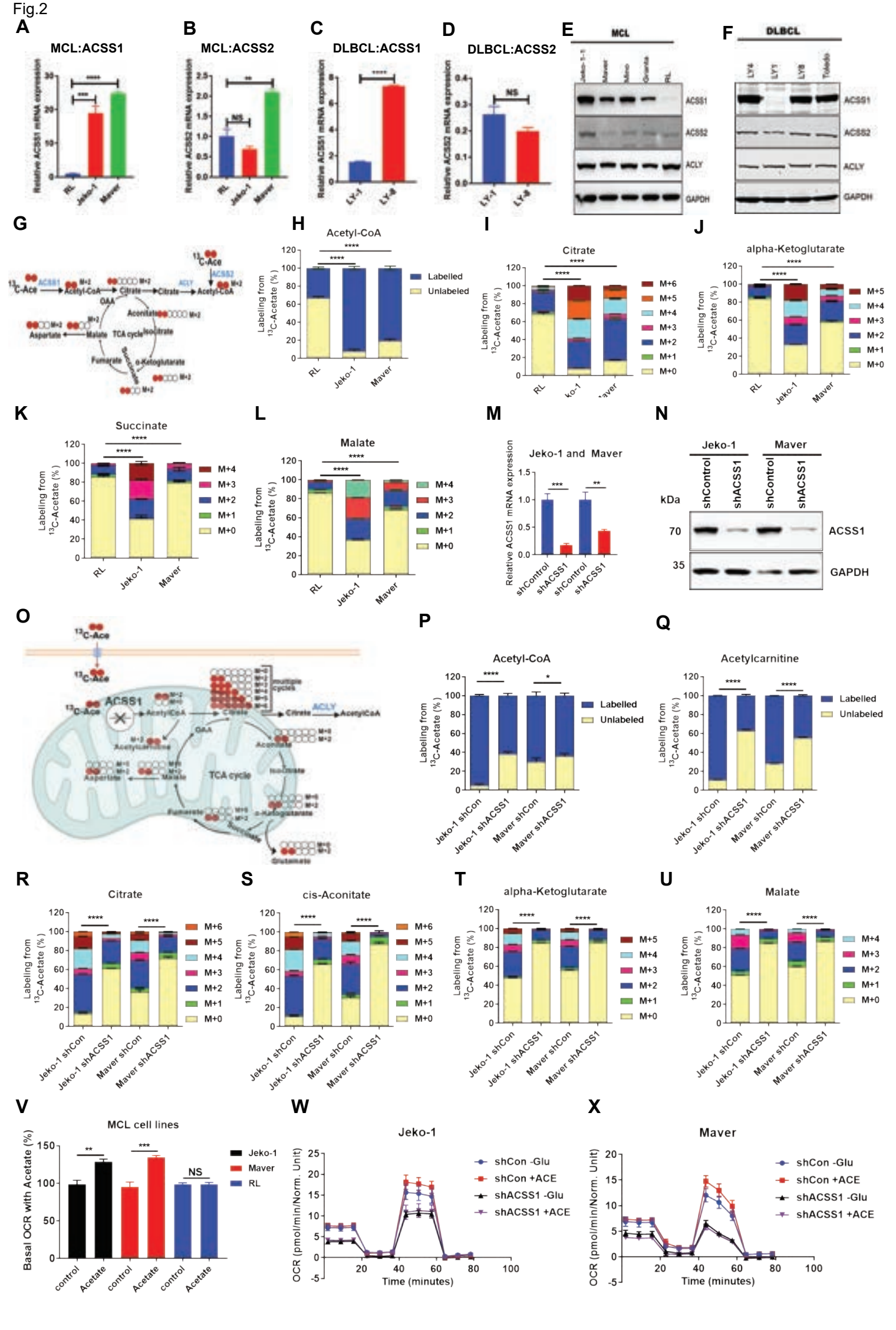
A
MCL:ACSS1
Relative ACSS1 mRNA expression
RL
Jeko-1
Maver
B
MCL:ACSS2
Relative ACSS2 mRNA expression
NS
C
DLBCL:ACSS1
LY-1
LY-8
D
DLBCL:ACSS2
E
MCL
ACSS1
ACSS2
ACLY
GAPDH
F
DLBCL
G
H
Acetyl-CoA
Labelled
Unlabeled
I
Citrate
J
alpha-Ketoglutarate
K
Succinate
L
Malate
M
Jeko-1 and Maver
shControl
shACSS1
N
Jeko-1
Maver
kDa
70
35
O
P
Acetyl-CoA
Q
Acetylcarnitine
R
Citrate
S
cis-Aconitate
T
alpha-Ketoglutarate
U
Malate
Jeko-1 shCon
Jeko-1 shACSS1
Maver shCon
Maver shACSS1
V
MCL cell lines
Basal OCR with Acetate (%)
control
Acetate
W
Jeko-1
X
Maver
shCon -Glu
shCon +ACE
shACSS1 -Glu
shACSS1 +ACE
OCR (pmol/min/Norm. Unit)
Time (minutes)

Fig. 3

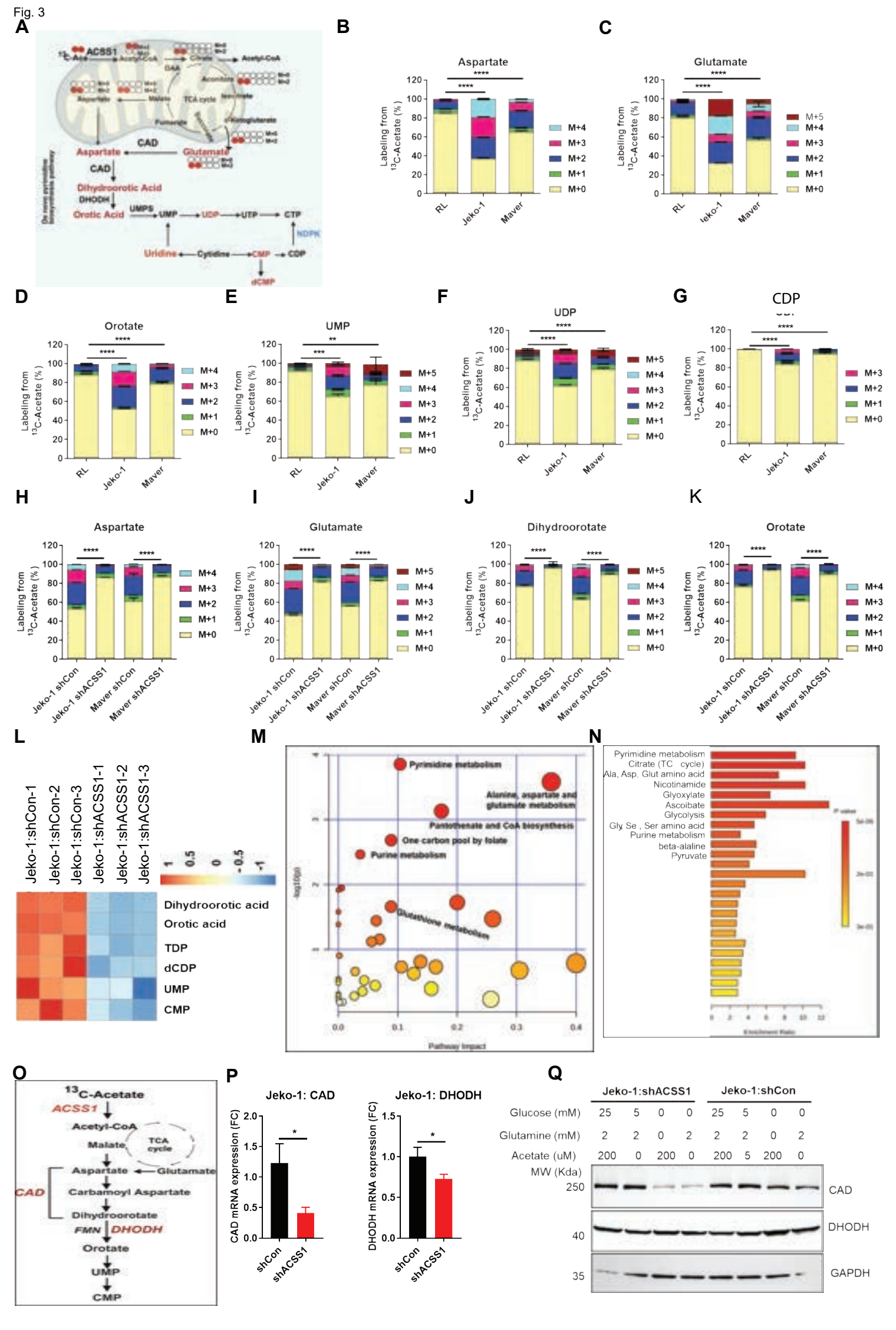
A
ACSS1
Acetyl-CoA
Citrate
Aconitate
Isocitrate
α-Ketoglutarate
Succinate
Fumarate
Malate
Aspartate
TCA cycle
CAD
Glutamate
Dihydroorotic Acid
DHODH
Orotic Acid
UMPS
UMP
UDP
UTP
CTP
NDPK
Uridine
Cytidine
CMP
CDP
dCMP
B
Aspartate
C
Glutamate
Labeling from 13C-Acetate (%)
RL
Jeko-1
Maver
M+5
M+4
M+3
M+2
M+1
M+0
D
Orotate
E
UMP
F
UDP
G
CDP
H
Aspartate
I
Glutamate
J
Dihydroorotate
K
Orotate
Jeko-1 shCon
Jeko-1 shACSS1
Maver shCon
Maver shACSS1
L
Jeko-1:shCon-1
Jeko-1:shCon-2
Jeko-1:shCon-3
Jeko-1:shACSS1-1
Jeko-1:shACSS1-2
Jeko-1:shACSS1-3
Dihydroorotic acid
Orotic acid
TDP
dCDP
UMP
CMP
M
Pyrimidine metabolism
Alanine, aspartate and glutamate metabolism
Pantothenate and CoA biosynthesis
One carbon pool by folate
Purine metabolism
Glutathione metabolism
Pathway Impact
N
Pyrimidine metabolism
Citrate (TC cycle)
Ala, Asp, Glut amino acid
Nicotinamide
Glyoxylate
Ascoibate
Glycolysis
Gly, Se , Ser amino acid
Purine metabolism
beta-alaline
Pyruvate
O
13C-Acetate
ACSS1
Acetyl-CoA
Malate
TCA cycle
Aspartate
Glutamate
CAD
Carbamoyl Aspartate
Dihydroorotate
FMN
DHODH
Orotate
UMP
CMP
P
Jeko-1: CAD
Jeko-1: DHODH
CAD mRNA expression (FC)
DHODH mRNA expression (FC)
shCon
shACSS1
Q
Jeko-1:shACSS1
Jeko-1:shCon
Glucose (mM)
Glutamine (mM)
Acetate (uM)
MW (Kda)
250
40
35
CAD
DHODH
GAPDH

Fig. 4

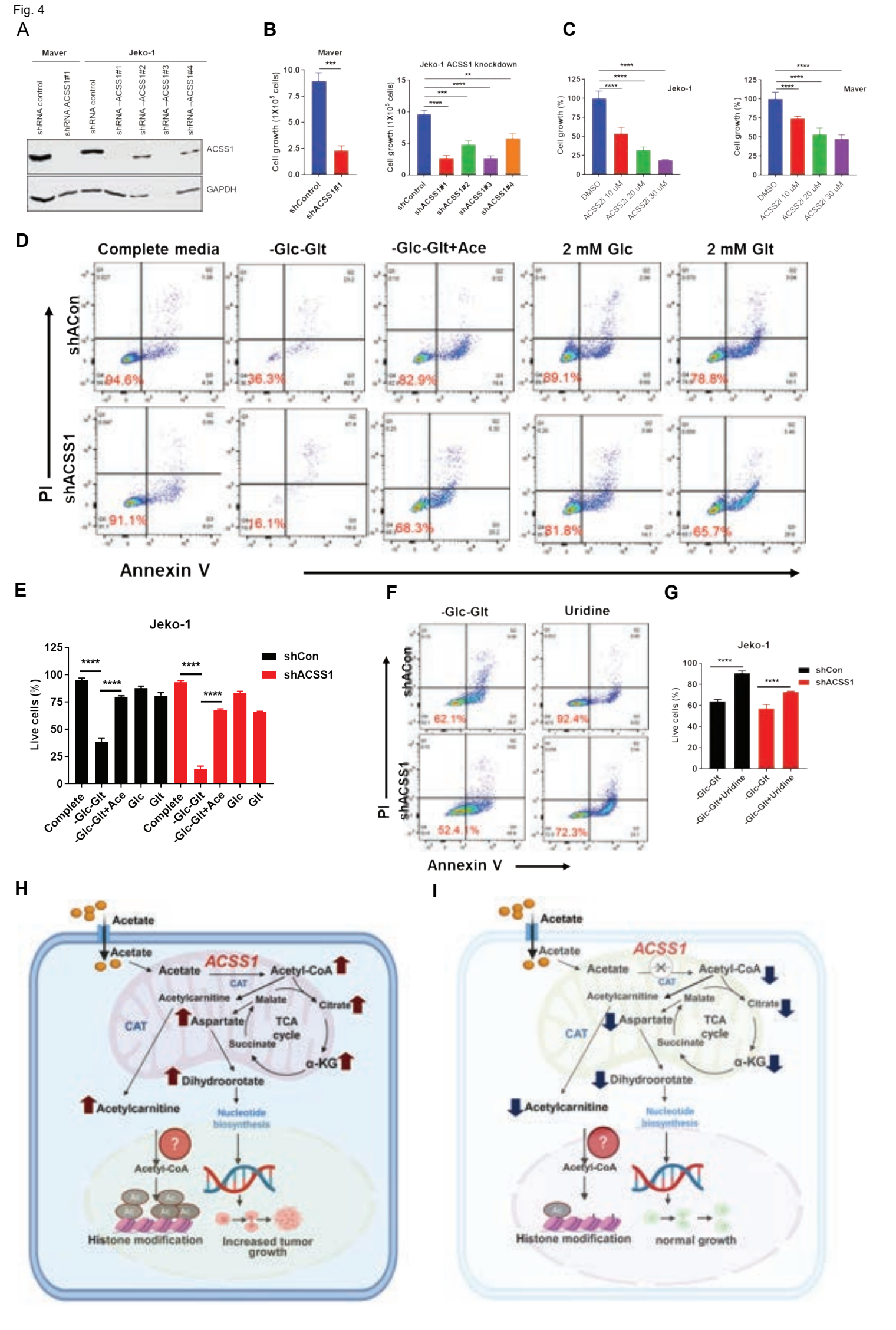
A
Maver
Jeko-1
shRNA control
shRNA ACSS1#1
shRNA control
shRNA –ACSS1#1
shRNA –ACSS1#2
shRNA –ACSS1#3
shRNA –ACSS1#4
ACSS1
GAPDH
B
Maver
Cell growth (1X10^5 cells)
shControl
shACSS1#1
Jeko-1 ACSS1 knockdown
shACSS1#2
shACSS1#3
shACSS1#4
C
Jeko-1
Maver
Cell growth (%)
DMSO
ACSS2i 10 uM
ACSS2i 20 uM
ACSS2i 30 uM
D
Complete media
-Glc-Glt
-Glc-Glt+Ace
2 mM Glc
2 mM Glt
shACon
shACSS1
PI
Annexin V
94.6%
36.3%
92.9%
89.1%
78.8%
91.1%
16.1%
68.3%
81.8%
65.7%
E
Jeko-1
Live cells (%)
shCon
shACSS1
Complete
-Glc-Glt
-Glc-Glt+Ace
Glc
Glt
F
-Glc-Glt
Uridine
62.1%
92.4%
52.4%
72.3%
G
Jeko-1
Live cells (%)
shCon
shACSS1
-Glc-Glt
-Glc-Glt+Uridine
H
Acetate
ACSS1
Acetyl-CoA
CAT
Acetylcarnitine
Malate
Citrate
Aspartate
TCA cycle
Succinate
α-KG
Dihydroorotate
Nucleotide biosynthesis
Histone modification
Increased tumor growth
I
normal growth

Supplementary Fig. 1

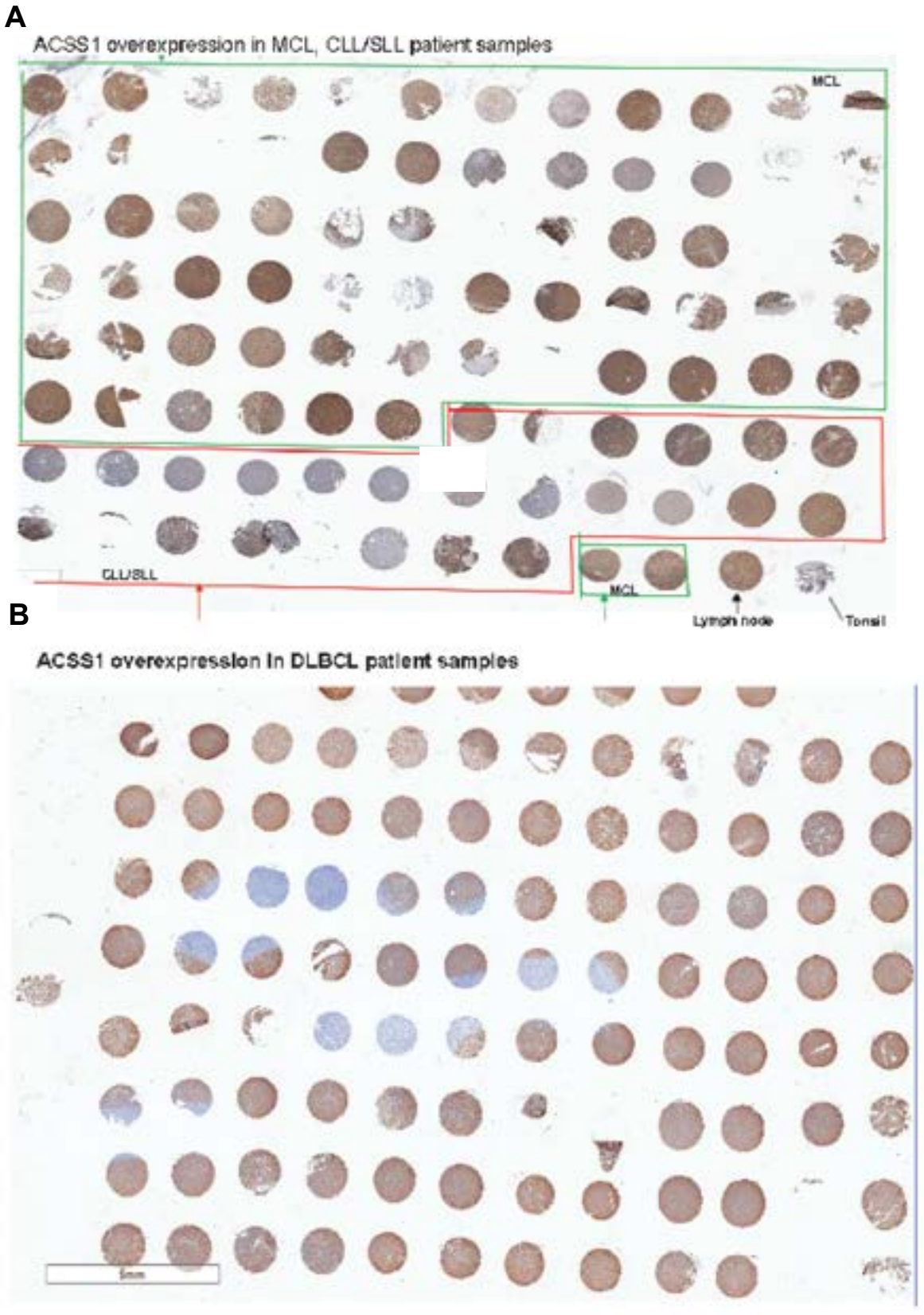

Immunohistochemistry (IHC) staining of ACSS1 in patients with MCL, DLBCL, and CLL biopsies.

A ACSS1 overexpression in MCL, CLL/SLL patient samples; **B** ACSS1 overexpression in DLBCL patient samples.

Supplementary Fig. 2

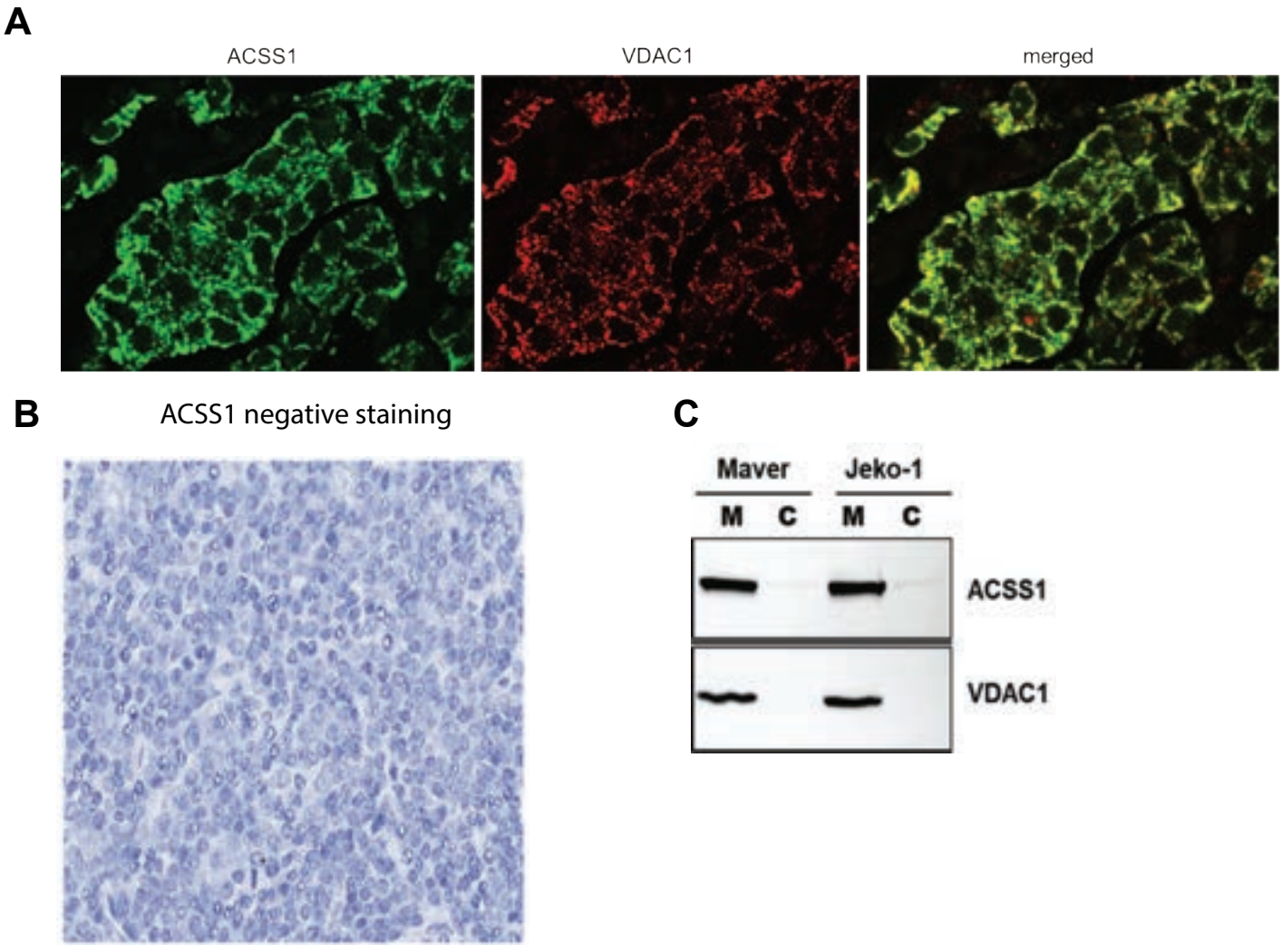

ACSS1 and VDAC1 co-localization in mitochondria.

A, Immunofluorescence (IF) on a human breast cancer patient sample with ACSS1 and VDAC1 staining, followed by confocal microscopy. **B**,Immunohistochemistry (IHC) negative staining of ACSS1 in MCL, DLBCL, and ALCL patient-derived TMA blocks. **C**, Mitochondrial fractionation of Jeko-1 and Maver cells.

Supplementary Fig. 3

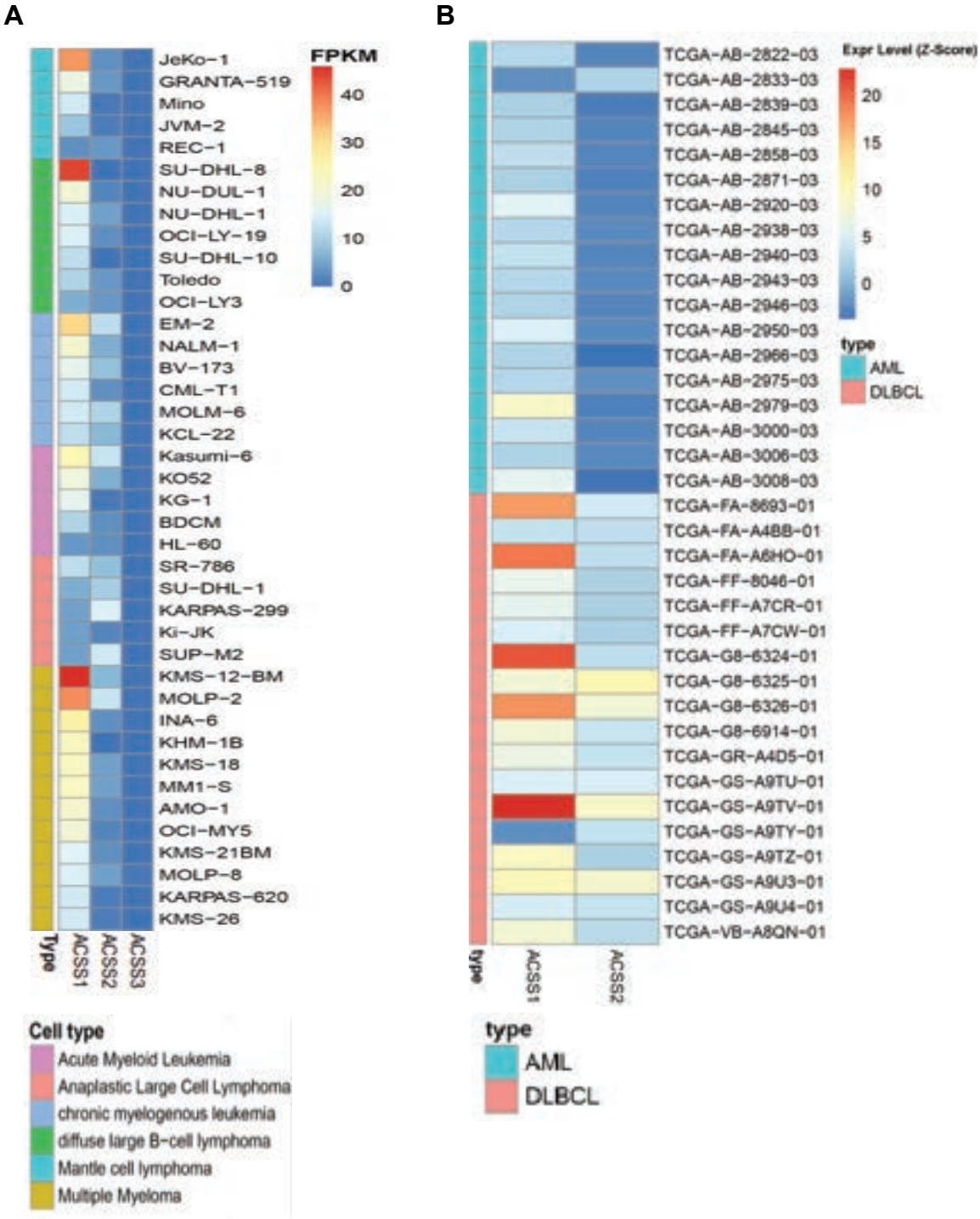

ACSS1 is overexpressed in cell lines and primary tissues derived from hematological malignancies.

A Targeted bioinformatics analysis of ACSS1, ACSS2, and ACSS3 gene expression deposited in the Expression Atlas database (https://www.ebi.ac.uk/gxa/home) revealed overexpression of ACSS1 in cell lines derived from human hematological malignancies (heat map); **B** The Cancer Genome Atlas (TCGA) database revealed ACSS1 overexpression in primary AML and DLBCL tissues.

Supplementary Fig. 4

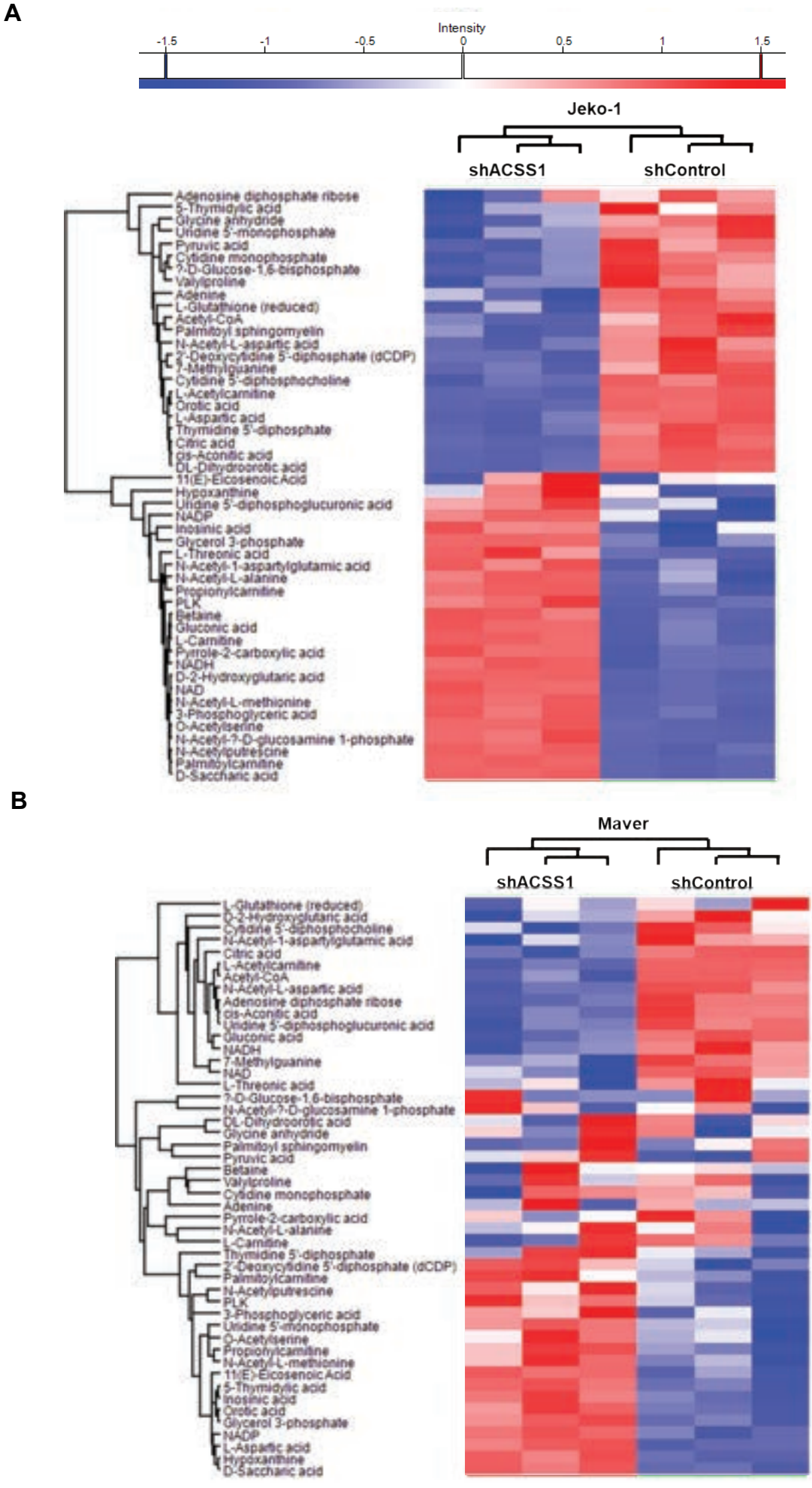

The steady-state metabolites significantly differed in Jeko-1 control compared to ACSS1 KD cell lines during nutrient deprivation.

a, b The heat map shows a statistically significant metabolite in shCon vs. shACSS1 in Jeko-1 and Maver cell lines.